Gu, YuanTong
(2008)
Geometrically nonlinear analysis of microswitches using the local mesh-free method.
International Journal of Computational Methods, *5*(4), pp. 513-532.

https://doi.org/10.1142/S0219876208001601

The geometrically nonlinear analysis of microswitches using the local meshfree method

Y. T. Gu
School of Engineering Systems
Queensland University of Technology
GPO Box 2434, Brisbane, QLD 4001 Australia
E-mail: yuantong.gu@qut.edu.au

ABSTRACT

In the modelling and simulation of the microelectromechanical systems (MEMS) devices, for example the microswitch, the large deformation or the geometrical nonlinearity should be considered. Due to the issue of the mesh distortion, the finite element method (FEM) is not effective for this large deformation analysis. In this paper, a local meshfree formulation is developed for the geometrically nonlinear analysis of MEMS devices. The moving least square approximation (MLSA) is employed to construct the meshfree shape functions based on the arbitrary distributed field nodes and the spline weight function. The discrete system of equations for two-dimensional MEMS analysis is obtained using the weighted local weak-form, and based on the total Lagrangian (TL) approach, which refers all variables to the initial configuration. The Newton-Raphson iteration technique is used to get final results. Several typical microswitches are simulated by the developed nonlinear local meshfree method. Some important parameters of these microswitches, e.g., the pull-in voltage, are studied. Comparing with the experimental results and results obtained by the linear analysis, the nonlinear meshfree analysis of microswitches is accurate and efficient. It has demonstrated that the present nonlinear local meshfree formulation is very effective for the geometrically nonlinear analysis of the MEMS devices, because it totally avoids the issue of mesh distortion in FEM.

KEYWORDS: MEMS, Microswitch, Meshfree method, Local weak-form, Geometrical nonlinearity, Large deformation

1. INTRODUCTION

Microelectromechanical systems (MEMS) have attracted a lot of attention due to its numerous applications in aerospace, automotive systems, manufacturing, and bioengineering[1]~[4]. The MEMS devices typically involve mixed energy domains including the electrical field, mechanical field, optical field, thermal field, etc. In addition, the geometrically nonlinear properties should be often considered in the deformation analysis of the MEMS devices due to the large deformation. For the numerical simulations of MEMS devices, the traditional finite element method (FEM) [5][6] is usually the dominant numerical technique. However, in the FEM analysis, the mesh generation is computationally expensive and mesh refinement is difficult, especially for problems with complicated geometries and multi-physical domains. In addition, due to the issue of the mesh distortion, FEM is ineffective for the geometrical nonlinearity when the deformation is large. Therefore, to overcome these issues, the meshfree (or meshless) method is a possible solution.

In recent years, more and more researchers are devoting themselves to the research of the meshfree methods, due to the fact that there are still many spaces in the development of meshfree methods. Detailed reviews of meshfree methods can be found in the monographs [7][8]. There are many categories of meshfree methods[8], and group of meshfree methods have been developed including the strong-form meshfree methods[9][10], the smooth particle hydrodynamics (SPH) [11], the element-free Galerkin (EFG) method [12][13], the reproducing kernel particle method (RKPM) [14][15], and the point interpolation method (PIM) [16]. In order to alleviate the global integration background cells, the meshfree methods based on the local weak-forms have also been developed, for example, the meshless local Petrov-Galerkin (MLPG) method [17]~[20], and the local radial point interpolation method (LRPIM) [21][22]. At the same time, the diverse meshfree methods have also been used for many applications in engineering and science [8].

However, there are still some critical issues in the development of meshfree methods. Many efforts have been put in recent years to study these issues. Liu [7] has explored the confirming issue in the meshfree interpolations and a linearly conforming point interpolation technique [23][24] has been proposed to overcome this issue. The convergent property of meshfree methods has also been studied [25][26], and the upper bound solution of the meshfree method has been obtained theoretically. In addition, Liu [27] proposed a generalized smoothed Galerkin weak-form that is applicable to create a wide class of efficient meshfree numerical methods with special properties including the upper bound properties. The above mentioned new advances are significant and resolve many issues, especially in theoretical aspects, in the development of meshfree methods.

Considering its distinguished advantages, the meshfree methods have very good potential for the numerical modelling and simulation of MEMS devices. Aluru and his colleagues developed a finite cloud meshfree method and applied it for the simulations of MEMS devices [28]. They have also used the RKPM (based of the strong-form) for the static and dynamic analyses of MEMS [29]. Wang et al. developed a so-called meshless point weighted least-squares method for MEMS analysis [30]. These meshfree methods are all based on the strong-forms. As many numerical techniques based on the strong-forms, these meshfree methods have also some inherent shortcomings including computational instability, inaccuracy, and difficulty in enforcement of boundary conditions (especially the derivative or Newman boundary conditions). The meshfree methods based on the local weak-forms, e.g., the meshfree local Petrov-Galerkin (MLPG) method [18], have many unique advantages, but they have not been used in the simulations of MEMS devices. In addition, the geometrically nonlinear analysis is a challenge for researchers in analysis of MEMS devices. Although FEM is a well-established mesh method, it often encounters difficulties for nonlinear analyses due to the issue of mesh distortion. Because no mesh is used, the meshfree methods show very good potential for the geometrically nonlinear analysis. The meshfree methods based on the global weak-forms have been successfully used in the geometrically nonlinear analysis. Chen et al. [31][32] concluded that the meshfree methods of EFG and RKPM (based on the global weak-forms) are very effective for the large deformation analyses. However, there is few study for the nonlinear analyses by the meshfree methods based on the local weak-forms [33], especially for the geometrical nonlinearity analysis of MEMS devices.

In this paper, a nonlinear local meshfree formulation is developed for the geometrically nonlinear analysis of MEMS devices, especially the microswitches. The problem domain of a microswitch is represented by reasonably distributed field nodes. The moving least squares approximation (MLSA) is employed to construct the meshfree shape functions based on the local interpolation domain and the spline weight function. The discrete system of equations for nonlinear analysis of the microswitch is obtained using the weighted local weak-forms, and based on the total Lagrangian (TL) approach [34], which refers all variables to the initial configuration. Newton-Raphson iteration technique is used to get final results. Several typical microswitches are simulated by the newly developed nonlinear local meshfree method, and some important parameters for these microswitches, e.g., the critical pull-in voltages, are studied. Comparing with the experimental results and results in the linear analysis obtained by other methods, it has proven that the developed meshfree formulation is very effective for the geometrically nonlinear analysis of the MEMS devices.

2. NONLINEAR LOCAL MESHFREE FORMULATION

2.1. Microswitches

In the analysis of MEMS devices, the multi-domain problems are usually considered because these devices often involve electric, mechanical, optical, and thermal fields. In addition, the analyzed problems are often nonlinear, because of not only the nonlinear loading, but also the geometrical nonlinearity induced by the large deformation. The microswitch is one of the most typical MEMS devices. As an example, Figures 1 and 2 show a fixed-fixed microswitch and a cantilever microswitch, respectively. These microswitches are constructed by deformable switch arms and the undeformable bottom electrode. Under the applied voltage, the arm of the microswitch will deflect (as shown in Figures 1(b) and 2(b)), and the gap between the arm and the bottom electrode changes. The electrostatic force induced by the applied voltage can be expressed as [28]

$$\mathbf{b} = -J\mathbf{F}^{-T}\mathbf{N}\frac{\varepsilon_0 V^2 h}{2g^2}\left(1+0.65\frac{g}{h}\right) \tag{1}$$

where ε_0 is the permittivity of vacuum, V is applied voltage, h is the arm width, and g is the gap between the arm and the bottom electrode, $g = g_0 - u_y$, where g_0 is the initial distance between the undeformed arm and the bottom electrode, **F** is the deformation gradient (which will be given in the following session), J is the determinant of **F**, and **N** is the surface normal of the initial configuration. It can be found from Eq. (1) that the above force is a nonlinear function of deflection.

In the simulation of the microswitch, the electrostatic pull-in characteristic is a well-known sharp instability in the behavior of an elastically supported structure subjected to parallel-plate electrostatic actuation. As the applied voltage increases, the deflection of the switch arm increases, and the gap between the arm and the bottom electrode decreases. It has been reported that when the applied voltage increases to one certain value, the arm becomes unstable and the centre of the arm (for fixed-fixed switch) or the free end of the arm (for the cantilever switch) will touch the bottom electrode (i.e., the gap is 0). This process is defined as the pull-in behavior and the “certain value” of the applied voltage is defined as the quasi-static critical pull-in voltage[1] [28][30].

2.2. Nonlinear local weak-forms

Consider a body, which occupies a region ${}_0\Omega$ at the initial stage and occupies a region ${}_t\Omega$ at the step t. The deformation of a material particle $\mathbf{X} \in {}_0\Omega$ at time t is described by $\mathbf{x}(\mathbf{X},t) \in {}_t\Omega$ through the mapping functions $\boldsymbol{\varphi}$, and we have [35]

$$\mathbf{u}(\mathbf{X},t) = \mathbf{x}(\mathbf{X},t) - \mathbf{X} \tag{2}$$

where $\mathbf{u}$ is the displacement of this material particle. A fundamental measure of deformation is described by the deformation gradient, $\mathbf{F}$, relative to $\mathbf{X}$ given by

$$\mathbf{F} = \frac{\partial \mathbf{x}}{\partial \mathbf{X}} = \frac{\partial(\mathbf{X} + \mathbf{u}(\mathbf{X},t))}{\partial \mathbf{X}} = \frac{\partial \mathbf{u}}{\partial \mathbf{X}} + \boldsymbol{\delta}\text{, and } J = |\mathbf{F}| > 0 \tag{3}$$

Using the variables related to the current configuration, at step t, the standard equilibrium equation and boundary conditions for a solid are given by

$$\sigma_{ij,j} + \rho b_i = 0 \qquad \text{in } {}_t\Omega \tag{4}$$

$$\sigma_{ij} n_j \quad \bar{t}_i \quad on \quad {}_t\Gamma_t \tag{5}$$

$$u_i = \bar{u}_i \quad on \quad {}_t\Gamma_u \tag{6}$$

where σ is the Cauchy stress tensor, b is the body force per unit mass and ρ is the mass density in the current configuration ${}_t\Omega$, n is the unit outward normal on the deformed surface, and $\bar{u}_i$ and $\bar{t}_i$ are prescribed displacements and tractions on the boundaries ${}_t\Gamma_u$ and ${}_t\Gamma_t$ of the current configuration ${}_t\Omega$. In the current configuration, a symmetric measure of stress, the Cauchy (true) stress, σ, is often employed, which is the work conjugate of the rate-of-deformation, expressed as the symmetric part of Kirchhoff stress, τ, and

$$\tau_{ij} = J\sigma_{ij} = F_{iI} S_{IJ} F_{jJ} \tag{7}$$

where S is the second Piola-Kirchhoff stress.

For a field node L, Eq. (4) is satisfied by using the Petrov-Galerkin formulation over a local quadrature domain ${}_t\Omega_q$ bounded by ${}_t\Gamma_q$, as shown in Figure 3, and leads to a weighted local weak-form equation for this node, i.e.,

$$\int_{{}_t\Omega_q} w_L (\sigma_{ij,j} + \rho b_i) \mathrm{d}\,{}_t\Omega = 0 \tag{8}$$

where w_L is the weight or weight function centered usually at node L The first part on the left-hand side of Eq. (8) can be integrated by parts to obtain

$$\int_{{}_t\Gamma_q} w_L \sigma_{ij} n_j \mathrm{d}_t\Gamma - \int_{{}_t\Omega_q} \left[w_{L,j}\sigma_{ij} - v_L \rho b_i \right] \mathrm{d}_t\Omega = 0 \tag{9}$$

Usually, the boundary ${}_t\Gamma_q$ for the local quadrature domain, ${}_t\Omega_q$, is composed by three parts [8], i.e., ${}_t\Gamma_q = {}_t\Gamma_{qi} \cup {}_t\Gamma_{qu} \cup {}_t\Gamma_{qt}$, where ${}_t\Gamma_{qi}$ is the internal boundary of the quadrature domain, which does not intersect with the global boundary ${}_t\Gamma$; ${}_t\Gamma_{qt}$ is the part of the natural boundary that intersects with the quadrature domain, and ${}_t\Gamma_{qu}$ is the part of the essential boundary that intersects with the quadrature domain. Because it is easy to construct a weight function with a desired order of continuity using the spline weight function, the quartic spline weight functions are used for w_L. The spline weight function can be purposely selected so that the integral on ${}_t\Gamma_{qi}$ vanishes to simplify the local weak-form. If the weight function satisfies this property, the local weak-form of Eq. (9) can be re-written as

$$\int_{{}_t\Omega_q} w_{L,j}\sigma_{ij} \mathrm{d}_t\Omega - \int_{{}_t\Omega_q} w_L \rho b_i \mathrm{d}_t\Omega - \int_{{}_t\Gamma_{qu}} w_L \sigma_{ij} n_j \mathrm{d}_t\Gamma - \int_{{}_t\Gamma_{qt}} w_L \bar{t}_i \mathrm{d}_t\Gamma = 0 \tag{10}$$

Due to the deformed configuration is unknown, the total Lagrangian (TL) formulation, which refers all stresses and deformations to the initial undeformed (reference) configuration at time t=0, is used. Eq. (10) can be re-written using the following matrix form

$$\int_{{}_0\Omega_q} \mathbf{vFS}\mathrm{d}\Omega - \int_{{}_0\Gamma_{qi}+{}_0\Gamma_{qu}} \mathbf{wNFS}\mathrm{d}\Gamma = \int_{{}_0\Gamma_{qt}} \mathbf{w\bar{T}}\mathrm{d}\Gamma + \int_{{}_0\Omega_q} \boldsymbol{\rho}\mathbf{wb}\mathrm{d}\Omega \tag{11}$$

To handle the geometric nonlinearity, the incremental formulation is usually used [34][35]. For the reference (undeformed) configuration during a finite deformation, we have the following incremental relationships

$${}^{t+\Delta t}_{0}\mathbf{u} = {}^{t}_{0}\mathbf{u} + \Delta\mathbf{u} \tag{12}$$

$${}^{t+\Delta t}_{0}\mathbf{S} = {}^{t}_{0}\mathbf{S} + \Delta\mathbf{S} \tag{13}$$

$${}^{t+\Delta t}_{0}\mathbf{F} = \frac{\partial({}^{t+\Delta t}_{0}\mathbf{u})}{\partial\mathbf{X}} + \boldsymbol{\delta} = {}^{t}_{0}\mathbf{F} + \frac{\partial({}^{t}_{0}\mathbf{u})}{\partial\mathbf{X}} = {}^{t}_{0}\mathbf{F} + \Delta\mathbf{F} \tag{14}$$

where $\Delta\mathbf{u}$, $\Delta\mathbf{S}$ and $\Delta\mathbf{F}$ are the increments of the displacement, second Piola-Kirchhoff stress and the deformation gradient, respectively. Substituting Eqs. (12)~(14) into Eq. (11), we can obtain the following incremental local weak-form in the matrix form

$$\int_{{}_0\Omega_q} \mathbf{v}_L \, {}_0^t\mathbf{F} \, {}_0^t\mathbf{D}\Delta\mathbf{E}\mathrm{d}\Omega + \int_{{}_0\Omega_q} \mathbf{v}_L \, {}_0^t\mathbf{S}\Delta\mathbf{F}\mathrm{d}\Omega - \int_{{}_0\Gamma_{qi}+{}_0\Gamma_{qu}} \mathbf{w}_L \, {}_0^t\mathbf{N} \, {}_0^t\mathbf{F} \, {}_0^t\mathbf{D}\Delta\mathbf{E}\mathrm{d}\Gamma \tag{15}$$
$$- \int_{{}_0\Gamma_{qi}+{}_0\Gamma_{qu}} \mathbf{w}_L \, {}_0^t\mathbf{N} \, {}_0^t\mathbf{S}\Delta\mathbf{F}\mathrm{d}\Gamma$$
$$= \int_{{}_0\Gamma_{qt}} \mathbf{w}_L \, {}_0^t\overline{\mathbf{T}}\mathrm{d}\Gamma + \int_{{}_0\Omega_q} \mathbf{w}_L \boldsymbol{\rho}\mathbf{b}\mathrm{d}\Omega + \int_{{}_0\Gamma_{qi}+{}_0\Gamma_{qu}} \mathbf{w}_L \, {}_0^t\mathbf{N} \, {}_0^t\mathbf{F}\widehat{\mathbf{S}}\mathrm{d}\Gamma - \int_{{}_0\Omega_q} \mathbf{v}_L \, {}_0^t\mathbf{F} \, {}_0^t\widehat{\mathbf{S}}\mathrm{d}\Omega$$

where $\mathbf{v}$ is the matrix for the derivatives of the weight functions, $\mathbf{F}$ is the deformation gradient matrix, $\Delta\mathbf{E}$ is the vector for the increments of Green strains, $\mathbf{S}$ and $\widehat{\mathbf{S}}$ are the matrix and the vector, respectively, of the second Piola-Kirchhoff stress, $\mathbf{N}$ is the matrix of the unit outward normal with respect to the reference configuration, and $\mathbf{D}$ is the material moduli with respect to the reference configuration.

2.3. Discretization formulations

For discretization, the problem domain is represented by a group of field nodes. The well developed moving least square approximation (MLSA)[36] is used in this paper. Consider a problem domain Ω, a approximated function $u^h(\mathbf{x})$ for a function $u(\mathbf{x})$ at a sample point $\mathbf{x}$ is defined by

$$u^h(\mathbf{x}) = \sum_{j=1}^{m} p_j(\mathbf{x}) a_j(\mathbf{x}) = \mathbf{p}^{\mathrm{T}}(\mathbf{x})\mathbf{a}(\mathbf{x}) \tag{16}$$

where $\mathbf{p}(\mathbf{x})$ is a vector of polynomial basis functions, m is the number of basis functions, and $\mathbf{a}(\mathbf{x})$ is a coefficient vector. $\mathbf{a}(\mathbf{x})$ can be obtained by minimizing a weighted discrete $\mathbf{L}_2$ norm of:

$$J = \sum_{i=1}^{n} \widehat{w}(\mathbf{x}-\mathbf{x}_i)[\mathbf{p}^{\mathrm{T}}(\mathbf{x}_i)\mathbf{a}(\mathbf{x}) - u_i]^2 \tag{17}$$

where n is the number of nodes in the local support domain of $\mathbf{x}$ for which the weight function $\widehat{w}(\mathbf{x}-\mathbf{x}_i) \neq 0$, and u_i is the nodal value of u at $\mathbf{x}=\mathbf{x}_i$.

The stationarity of J with respect to $\mathbf{a}(\mathbf{x})$ leads to the following linear relation between $\mathbf{a}(\mathbf{x})$ and $\mathbf{u}_e$:

$$\mathbf{A}(\mathbf{x})\mathbf{a}(\mathbf{x})=\mathbf{B}(\mathbf{x})\mathbf{u}_e \tag{18}$$

where $\mathbf{A}(\mathbf{x})$ is called the moment matrix. $\mathbf{A}$ and $\mathbf{B}$ are defined by

$$\mathbf{A}(\mathbf{x}) = \sum_{i=1}^{n} \widehat{w}_i(\mathbf{x})\mathbf{p}(\mathbf{x}_i)\mathbf{p}^{\mathrm{T}}(\mathbf{x}_i), \quad \widehat{w}_i(\mathbf{x}) = \widehat{w}(\mathbf{x}-\mathbf{x}_i) \tag{19}$$

$$\mathbf{B}(\mathbf{x})=[\hat{w}_1(\mathbf{x})\mathbf{p}(\mathbf{x}_1),\ \hat{w}_2(\mathbf{x})\mathbf{p}(\mathbf{x}_2),\ldots,\ \hat{w}_n(\mathbf{x})\mathbf{p}(\mathbf{x}_n)] \tag{20}$$

Solving $\mathbf{a}$(x) from Eq. (18) and substituting it into Eq. (16), we can get the MLSA shape function ϕ_i(x) is defined by

$$\mathbf{\Phi}^T = \mathbf{p}^T(\mathbf{x})\mathbf{A}^{-1}(\mathbf{x})\mathbf{B}(\mathbf{x}) \tag{21}$$

The MLSA approximation is obtained by a special least squares method. The function obtained by the MLSA is a smooth curve (or surface) and it does not pass through the nodal values. Therefore, the MLSA shape functions do not, in general, have the Kronecker delta property [8]. The essential boundary conditions are usually enforced by the direct collocation method or the penalty method [19]. In this paper, the penalty technique is used to enforce the essential boundary conditions, because it is simple and efficient[8]. It should be also mentioned here that if the proper weight function is used in the MLSA approximation, the MLSA shape functions satisfy the continuity in the global domain[8].

Using the meshfree shape functions obtained above, the displacement vector $\mathbf{u}$ can be approximated by

$$\mathbf{u} = \sum_{i=1}^{n} \mathbf{\Phi}_i \mathbf{u}_i \tag{22}$$

where $\mathbf{\Phi}$ is the matrix of the MLSA shape functions.

Substituting Eq. (22) into Eq. (15), we can obtain the discretized system of equations for the field node L

$$\mathbf{K}_L \Delta\mathbf{U} = \mathbf{P}_L, \qquad L=1\sim N \text{ (N is the number of total field nodes)} \tag{23}$$

where

$$\begin{aligned}\mathbf{K}_L = &\int_{{}_0\Omega_q} \mathbf{v}_L\, {}_0^t\mathbf{F}\, {}_0^t\mathbf{D}\mathbf{B}^{nl}\mathrm{d}\Omega + \int_{{}_0\Omega_q} \mathbf{v}_L\, {}_0^t\mathbf{S}\mathbf{B}^{l}\mathrm{d}\Omega \\ &- \int_{{}_0\Gamma_{qi}+{}_0\Gamma_{qu}} \mathbf{w}_L\, {}_0^t\mathbf{N}\, {}_0^t\mathbf{F}\, {}_0^t\mathbf{D}\mathbf{B}^{nl}\mathrm{d}\Gamma - \int_{{}_0\Gamma_{qi}+{}_0\Gamma_{qu}} \mathbf{w}_L\, {}_0^t\mathbf{N}\, {}_0^t\mathbf{S}\mathbf{B}^{l}\mathrm{d}\Gamma\end{aligned} \tag{24}$$

$$\mathbf{P}_L = \int_{{}_0\Gamma_{qt}} \mathbf{w}_L\, {}_0^t\bar{\mathbf{T}}\mathrm{d}\Gamma + \int_{{}_0\Omega_q} \mathbf{w}_L \boldsymbol{\rho}_0 \mathbf{b}\mathrm{d}\Omega + \int_{{}_0\Gamma_{qi}+{}_0\Gamma_{qu}} \mathbf{w}_L\, {}_0^t\mathbf{N}\, {}_0^t\mathbf{F}\, {}_0^t\hat{\mathbf{S}}\mathrm{d}\Gamma - \int_{{}_0\Omega_q} \mathbf{v}_L\, {}_0^t\mathbf{F}\, {}_0^t\hat{\mathbf{S}}\mathrm{d}\Omega \tag{25}$$

where $\mathbf{D}$ is the material matrix, $\mathbf{F}$ is the deformation gradient matrix, $\mathbf{S}$ and $\hat{\mathbf{S}}$ are, respectively, the matrix and the vector of the second Piola-Kirchhoff stress. Other matrices and vectors are given as [33]

$$\mathbf{v}_L = \begin{bmatrix} w_{,x} & 0 & w_{,y} \\ 0 & w_{,y} & w_{,x} \end{bmatrix}, \qquad \mathbf{w}_L = \begin{bmatrix} w & 0 \\ 0 & w \end{bmatrix} \tag{26}$$

$$\mathbf{N} = \begin{bmatrix} N_x & 0 & N_y \\ 0 & N_y & N_x \end{bmatrix}, \quad \bar{\mathbf{T}} = \begin{Bmatrix} \bar{T}_x \\ \bar{T}_y \end{Bmatrix}, \quad \mathbf{b} = \begin{Bmatrix} b_x \\ b_y \end{Bmatrix} \tag{27}$$

$$\mathbf{B}^l = \begin{bmatrix} \frac{\partial \phi_1}{\partial X} & 0 & \cdots & \frac{\partial \phi_n}{\partial X} & 0 \\ 0 & \frac{\partial \phi_1}{\partial Y} & \cdots & 0 & \frac{\partial \phi_n}{\partial Y} \\ \frac{\partial \phi_1}{\partial Y} & 0 & \cdots & \frac{\partial \phi_n}{\partial Y} & 0 \\ 0 & \frac{\partial \phi_1}{\partial X} & \cdots & 0 & \frac{\partial \phi_n}{\partial X} \end{bmatrix} \tag{28}$$

$$\mathbf{B}^{nl} = \begin{bmatrix} F_{11}\frac{\partial \phi_1}{\partial X} & F_{21}\frac{\partial \phi_1}{\partial X} & \cdots & F_{11}\frac{\partial \phi_n}{\partial X} & F_{21}\frac{\partial \phi_n}{\partial X} \\ F_{12}\frac{\partial \phi_1}{\partial Y} & F_{22}\frac{\partial \phi_1}{\partial Y} & \cdots & F_{12}\frac{\partial \phi_n}{\partial Y} & F_{22}\frac{\partial \phi_n}{\partial Y} \\ F_{11}\frac{\partial \phi_1}{\partial Y} + F_{12}\frac{\partial \phi_1}{\partial X} & F_{21}\frac{\partial \phi_1}{\partial Y} + F_{22}\frac{\partial \phi_1}{\partial X} & \cdots & F_{11}\frac{\partial \phi_n}{\partial Y} + F_{12}\frac{\partial \phi_n}{\partial X} & F_{21}\frac{\partial \phi_n}{\partial Y} + F_{22}\frac{\partial \phi_n}{\partial X} \end{bmatrix} \tag{29}$$

In Eq. (25), **b** in the second item is the nonlinear function of the displacement (see Eq. (1)); the third and the fourth items are also function of displacements. Hence, Eq. (23) is nonlinear. The Newton-Raphson iteration technique [34] is often used to get results in the geometrically nonlinear analysis of microswitches.

3. NUMERICAL EXEMPLE

3.1. Validation by a large deformation analysis of a cantilever beam

In order to validate the present nonlinear local meshfree formulation, a benchmark problem of a cantilever beam is studied firstly. For this beam, the compressible hyperelastic neo-Hookean material [34] is used with Lamé constants $\mu = 0.5\times10^4$ and $\lambda = 3.3\times10^3$. Except when mentioned, the units are taken as standard international units in the following examples.

As shown in Figure 4, the length of the cantilever beam is 10, and the height of the beam is 2. The plane strain state is considered, and the beam is subjected to a distributed vertical loading along the right end. The nonlinear analysis is carried out using load incremental steps

N and the load-scaling factor is β=10.0. It means that at the kth loading step, the distributed loading is f_k=10k/Unit.

To study the accuracy and stability, we also solve this problem by FEM with a fine mesh (with 738 degrees of freedom), and the FEM result is taken as the reference solution[33]. Figure 5 plots the FEM reference results of loading steps N=8. The following norm is defined as an error indicator,

$$e_u = \frac{\left| u_{(t)}^{Num} - u_{(t)}^{Ref} \right|}{\left| u_{(t)}^{Ref} \right|} \tag{30}$$

where $u_{(t)}^{Num}$ and $u_{(t)}^{Ref}$ are displacements obtained by the numerical method and the FEM reference solution, respectively. For easy comparisons, the vertical displacement, u_y, at point A (shown in Figure 4) is used.

Table 1 lists vertical displacements at Point A obtained by the presented nonlinear local meshfree method and the traditional FEM (using the same 33 nodes). The computational errors, which are given in Eq. (30), are also listed in this table.

Table 1 Vertical displacements u_y at Point A

Loading steps		N=1	N=2	N=3	N=4	N=5	N=6	N=7	N=8
Reference solution	- u_y	0.816	1.617	2.376	3.078	3.714	4.283	4.768	5.235
Meshfree	- u_y	0.791	1.574	2.301	3.03	3.663	4.253	4.785	5.251
	e_u(%)	3.06	2.66	3.16	1.56	1.37	0.70	0.36	0.31
FEM	- u_y	0.733	1.452	2.148	2.796	3.393	3.935	4.424	4.863
	e_u(%)	10.17	10.20	9.61	9.16	8.64	8.13	7.21	7.11

From this table, we can conclude that the present nonlinear local meshfree analysis leads to more accurate results than FEM when the same numbers of nodes are used. This is because the meshfree method has better accuracy than FEM[7], and it can also avoid the issue of mesh distortion in FEM.

Figure 6 plots the meshfree results for 20 loading steps using the regular nodes given in Figure 4. Compared with the reference FEM results shown in Figure 5 (for the first 8 loading steps), it can be found that the meshfree method leads very good results. It should be mentioned here that when N=20 the deflection at the free end of the beam is already about 4 times of the initial height of the beam. The large deformation does not affect the computational accuracy of the nonlinear meshfree analysis. It proves that the developed nonlinear local meshfree method is very effective for the large deformation analysis.

To test the stability of the developed method for irregularly nodal distributions, the computational model (as shown in Figure 7) using 128 irregular nodes is also studied. The deflection results are plotted in Figure 8 for eight loading steps. Compared with the reference FEM results given in Figure 5, it can be found that the present nonlinear local meshfree formulation also leads to very good results even using the irregularly nodal distribution. The stability for irregular nodes is one of attractive advantages of the local meshfree method.

3.2. Large deformation analysis for fixed-fixed microswitch

In this study, a fixed-fixed microswitch, as shown in Figure 1, is simulated. The switch arm has the parameters [1] [37] of: length=80 μm, width=10 μm, and thickness 0.5 μm. The initial gap g_0 between the beam and the bottom electrode is 0.7 μm. The Young's modulus E is 169 GPa, the Poisson's ratio is 0.3. Because the deflection of the switch arm is relatively large, the present nonlinear meshfree method is used to analyze this large deformation problem of this microswitch. It should be mentioned here that this problem is more complex than above beam problem studied in Session 3.1, because the loading (Eq. (1)) on the device is also nonlinear and it will be changed with the deflection. Hence, two Newton-Raphson iteration loops are required to get the solution: one for the nonlinear loading and the other for the geometrical nonlinearity.

As shown in Figure 9, the switch arm is represented by 259 irregularly distributed nodes. Figure 10 plots the deflections along the switch arm under different applied voltages. From Figure 11, we can obtain that the critical pull-in voltage for this microswitch is 15.14 volt. Compared with the critical pull-in value 15.17 volt obtained through the experiment and 15.1 volt obtained by FEM [1], the present nonlinear local meshfree method obtains good result. This device has also been analyzed by Wang et al. [30] using the linear theory. They obtained the critical pull-in voltage is 15.07 volt. Therefore, the nonlinear meshfree method gives more accurate result than the linear modelling.

To detailedly investigate the differences between linear and nonlinear analyses, the critical pull-in voltages for different initial gaps are obtained by the linear and the nonlinear meshfree analysis, respectively. Figure 12 plots the critical pull-in voltages obtained by both linear and nonlinear analysis. From this figure, we can find, for a small gap, the linear and nonlinear analyses give almost identical results, because for these cases the deflections are still in the range of small deformation. However, when the initial gap increases, the critical pull-in voltages obtained by linear and nonlinear analyses become significantly different due to the large deformation. The results obtained by the nonlinear analysis are usually larger than those obtained by the linear analysis. For the large deformation cases, the nonlinear local meshfree analysis will give more accurate results than the linear analysis.

3.3. Large deformation analysis for cantilever microswitch

Another microswitch—the cantilever microswitch as shown in Figure 2, which can be simplified as a cantilever beam, is also studied. The parameters for this cantilever microswitch are exactly same as those used in the fixed-fixed microswitch in the previous session. As the applied voltage increases, the deflection of the microswitch increases. Furthermore, the deflection at the free end, defined as peak deflection, increases largely. When the applied voltage reaches a certain value, the free end of the beam touches the bottom electrode.

Figures 13 and 14 plot the deflections along the switch arm under different applied voltages. Similarly, the critical pull-in voltage for this cantilever microswitch is 2.35 volt that is very close to the result of 2.33 volt obtained by the linear theory [30]. It should mentioned here that because the initial gap in this study is much smaller than the length and height, the linear and nonlinear analyses for this cantilever switch lead to very close results. When the initial gap becomes large, the nonlinear influence will become significant. Similarly, the results obtained by the nonlinear analysis are usually larger than those obtained by the linear analysis, but the difference between them for a cantilever microswitch is not significant as that for a fixed-fixed microswitch.

3.4. The microtweezer

A tungsten microtweezer [30], as shown in Figure 15, can be also considered as a microswitch. The parameters for this microtweezer arms are: 200μm long, 2.7μm wide and 2.5μm thick. The initial opening of the two arms, d_0, is 3μm. It was designed and simulated by MacDonald et al. [38] and Shi et al. [6]. In this nonlinear simulation, the microtweezer arms can be simplified as cantilever beams shown in Figure 15, and the effect of the coating layers is neglected. In the practical applications, there usually is an initial angle between the arms and the central line of the microtweezer, shown in Figure 15. For generalization, a microtweezer with an initial angle $\alpha = 0.5^{\circ}$ is simulated by the present nonlinear local meshfree method.

The work process of this microtweezer is: when the applied voltage is imposed on the arms, the arms begin to deflect and move to the central line. With the increase of the applied voltage, the deflections of the arms increase. When the voltage reaches one certain value, the tips of two arms contact with each other as shown in Figure 15. This value of the applied voltage is defined as the critical pull-in voltage or closing voltage.

Because of the symmetry of the microtweezer, only one arm is studied. The closing voltage obtained by the nonlinear local meshfree method is 155 volt, which agrees very well with the experimental result of 150 volt [38], and the other numerical result of 156–157 volt [6].

4. CONCLUSIONS

In this paper, a nonlinear local meshfree formulation is developed for the geometrically nonlinear analysis of the MEMS devices, especially the microswitch. The discrete system of equations is obtained using the weighted local weak-forms, and based on the total Lagrangian (TL) approach. Several typical microswitches are studied to illustrate the effectivity of the present method. Compared with the experimental results and the result obtained by other numerical methods, the present nonlinear local meshfree method leads to good results. From the studies in the paper, we draw the following conclusions:

a) The nonlinear local meshfree method is more effective than FEM for the geometrically nonlinear analysis, because it can fully overcome the issue of the mesh distortion in FEM.
b) In the modelling and simulation of the microelectromechanical systems (MEMS) devices, both geometrical and loading nonlinearity should be considered. For microswitches, the nonlinear influences will become significant when the initial gap and the deformation increase. The critical pull-in voltages obtained by the nonlinear analysis are usually larger than those obtained by the linear analysis. For the large deformation analysis, the nonlinear local meshfree method gives more accurate results than the linear analysis.
c) The nonlinear local meshfree method usually leads to good results for the numerical simulation of MEMS devices, and, hence, it has very good potential to become a powerful tool for modelling, simulation and design of the MEMS devices.

However, further research is required to make the present nonlinear local meshfree method as a practical simulation and design tool for MEMS devices, for example, the analysis of three-dimensional devices and the development of the commercial software package. In addition, the local week-form is usually not symmetric, which leads to poor computational efficiency. The symmetric Galerkin weak-form will be use in the future studies to overcome this issue.

ACKNOWLEDGEMENT

This work is supported by an ARC Discovery Grant.

REFERENCES

[1] Ananthasuresh G K, Gupta R K and Senturia S D 1996, An approach to macromodeling of MEMS for nonlinear dynamic simulation. Microelectromechanical Systems (MEMS), *ASME Dynamic Systems and Control (DSC) series*, 59, 401-407.

[2] Hung E S and Senturia S D 1999, Generating efficient dynamical models for microelectromechanical systems from a few finite-element simulation runs, *IEEE Journal of Microelectromechanical Systems*, 8(3), 280-289.

[3] Lyshevski S E2002, *MEMS and NEMS Systems, Devices, and Structures*. CRC Press, Boca Raton, Florida.

[4] Osterberg P M and Senturia S D 1997, M-TEST: a test chip for MEMS material property measurement using electrostatically actuated test structures, *Journal of Microelectromechanical Systems*, 6(2), 107-118.

[5] Senturia S D 1998, CAD challenges for microsensors, microactuators, and Microsystems, *Proc. IEEE*, 86, 1611-1626.

[6] Shi F, Ramesh P and Mukherjee S 1995, Simulation methods for micro-electro-mechanical structures (MEMS) with application to a microtweezer , *Computers and Structures*, 56 (5), 769-783.

[7] Liu G R 2002, *Meshfree methods: moving beyond the finite element method*. CRC press, Boca Raton, Florida.

[8] Liu G R and Gu Y T 2005, An introduction to meshfree methods and their programming. Springer Press, Berlin.

[9] Mai-Duy N and Tanner RI 2007 A collocation method based on one-dimensional RBF interpolation scheme for solving PDEs, *International Journal of Numerical Methods for Heat & Fluid Flow*, 17(2), 165-86

[10] Mai-Duy N (2006) An effective spectral collocation method for the direct solution of high-order ODEs, *Communications in Numerical Methods in Engineering*, 22(6),627-42

[11] Gingold R A and Monaghan J J 1977, Smooth particle hydrodynamics: theory and applications to non-spherical stars , *Monthly Notices of the Royal Astronomical Society*, 181, 375-389.

[12] Belytschko T, Lu Y Y and Gu L 1994, Element-free Galerkin methods , *International Journal for Numerical Methods in Engineering*, 37, 229-256.

[13] Kanok-Nukulchai W, Barry WJ and Saran-Yasoontorn K 2001 Meshless formulation for shear-locking free bending elements, *Structural engineering and Mechanics*, 11, 123-132.

[14] Liu WK, Jun S, Zhang Y 1995, Reproducing kernel particle methods. International Journal for Numerical Methods in Engineering, 20: 1081-1106.

[15] Aluru NR 1999 A reproducing kernel particle method for meshless analysis of microelectromechanical systems, *Computational Mechanics* , 23 (4), 324-338.

[16] Liu G R and Gu Y T, 2001, A point interpolation method for two-dimensional solid , *International Journal for Numerical Methods in Engineering*, 50, 937-951.

[17] Atluri S N and Zhu T 1998, A new meshless local Petrov-Galerkin (MLPG) approach in computational mechanics , *Computational Mechanics*, 22, 117-127.

[18] Atluri SN and Shen SP 2002, The Meshless Local Petrov-Galerkin (MLPG) method, Tech Sciemce Press. Encino USA.

[19] Atluri S N, Kim H G and Cho J Y 1999, A critical assessment of the truly meshless local Petrov-Galerkin (MLPG), and local boundary integral equation (LBIE) methods , *Computational Mechanics*, 24, 348-372.

[20] Gu Y T and Liu G R 2001, A meshless Local Petrov-Galerkin (MLPG) method for free and forced vibration analyses for solids , *Computational Mechanics*, 27(3), 188-198.

[21] Gu Y T and Liu G R 2001, A local point interpolation method for static and dynamic analysis of thin beams , *Computer Methods in Applied Mechanics and Engineering*, 190, 5515-5528.

[22] Liu G R and Gu Y T 2001, A local radial point interpolation method (LR-PIM) for free vibration analyses of 2-D solids , *Journal of Sound and Vibration*, 246 (1), 29-46.

[23] Zhang GY, Liu GR, Wang YY, Huang HT, Zhong ZH, Li GY, and Han X 2007, A linearly conforming point interpolation method (LC-PIM) for three-dimensional elasticity problems, *International Journal for Numerical Methods in Engineering*, 72, 1524-1543.

[24] Liu GR, Li Y, Dai KY, Luan MT and Xue W 2006, A Linearly conforming radial point interpolation method for solid mechanics problems, *International Journal of Computational Methods*, 3, 401-428.

[25] Liu GR and Zhang GY (2008), Upper bound solution to elasticity problems: a unique property of the linearly conforming point interpolation method (LC-PIM), *Int. J. Numer. Mech. Engrg*., 74, 1128-1161.

[26] Zhang GY, Liu GR, Nguyen TT, Song CX, Han X, Zhong ZH and Li GY 2007, The upper bound property for solid mechanics of the linearly conforming radial point interpolation method (LC-RPIM). *International Journal of Computational Methods*, 4(3): 521-541.

[27] Liu GR 2008, A generalized gradient smoothing technique and the smoothed bilinear form for Galerkin formulation of a wide class of computational methods, International Journal of Computational Methods, 5 (2), 199–236.

[28]Li G and Aluru N R 2001, Linear, nonlinear and mixed-regime analysis of electrostatic MEMS. Sensors and Actuators A, 91, 278-291.

[29]Aluru N R 1999, A reproducing kernel particle method for meshless analysis of microelectromechanical systems. Computational Mechanics, 23, 324-338.

[30] Wang QX, Li H and Lam KY 2007, Analysis of microelectromechanical systems (MEMS) devices by the meshless point weighted least-squares method. Comput. Mech. 40: 1–11

[31] Chen JS, Pan C, Wu C T and Liu WK 1996, Reproducing kernal perticle methods for large deformation analysis of nonlinear structures. Computer Methods in Applied Mechanics and Engineering, 139, 195-227.

[32] Chen JS, Pan C and Wu CT1997, Large deformation analysis of rubber based on a reproducing kernel particle method. Comp. Mech., 19, 153-168.

[33] Gu Y T, Wang Q X and Lam K Y 2007, A Meshless Local Kriging Method for large deformation Analyses. *Computer Methods in Applied Mechanics and Engineering*, 196, 1673–1684.

[34] Belytschko T, Liu WK and Moran B 2000, Nonlinear finite elements for continua and structures. John Wiley & Sons, Chichester

[35] Zienkiewicz OC and Taylor RL 2000, The finite element method (5th ed.). Butterworth Heinemann, Oxford.

[36] Lancaster P and Salkauskas K 1981, Surface generated by moving least squares methods. Math. Comput., 37, 141-158.

[37] Wang QX, Hua L, Lam KY, Gu Y T 2004, Analysis of microelectromechanical systems (MEMS) by meshless local kriging (Lokriging) method, Journal of the Chinese Institute of Engineers, 4, 573-583.

[38] MacDonald N C, Chen L Y, Yao J J, Zhang J A, Mcmillan J A and Thomas D C 1989, Selective chemical vapor deposition of tungsten for microelectomechanical structures , *Sensors and Actuators*, 20, 123-133.

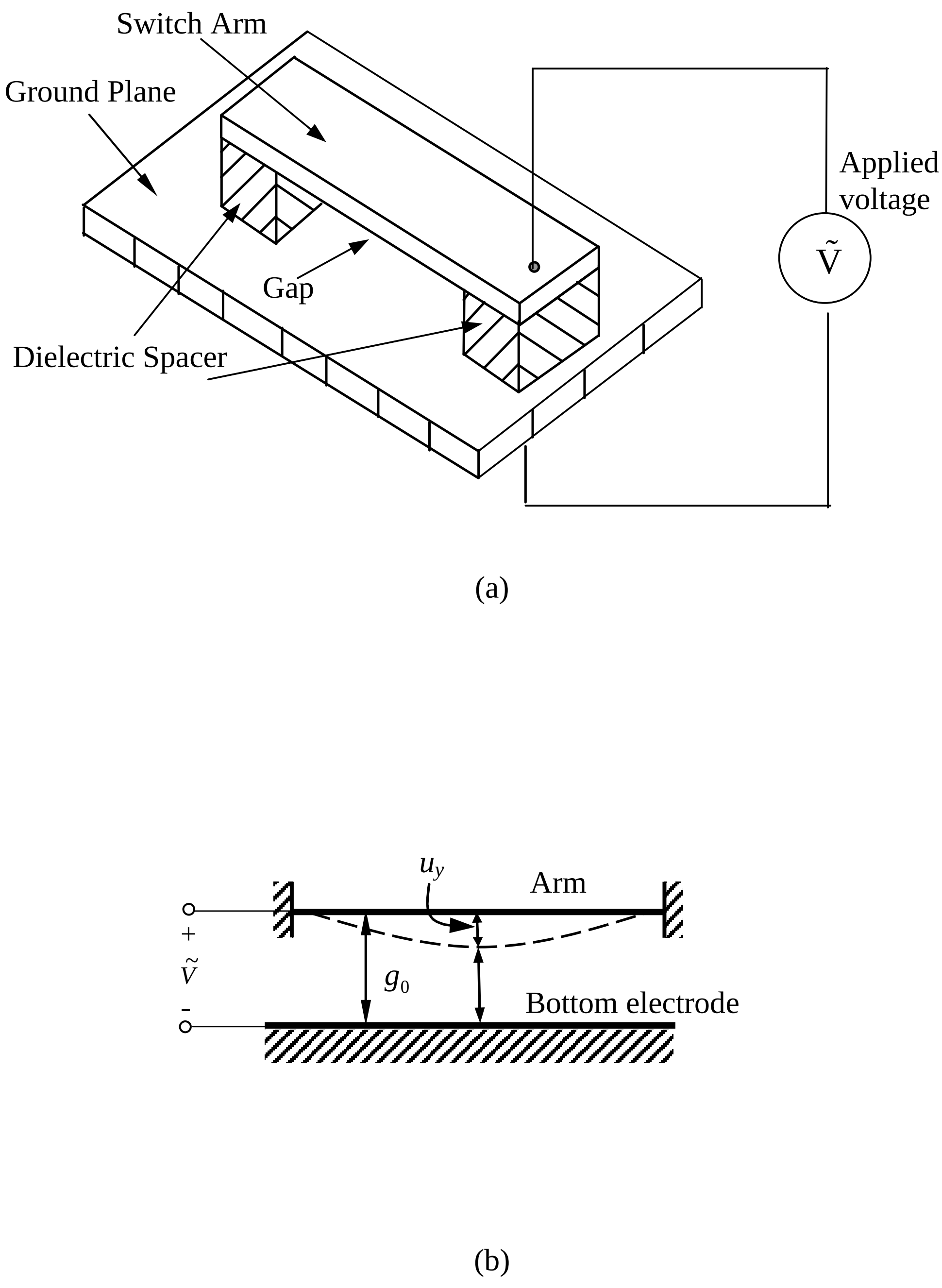

Figure 1 A fixed-fixed microswitch. a) Undeformed configuration; b) deformation under applied voltage

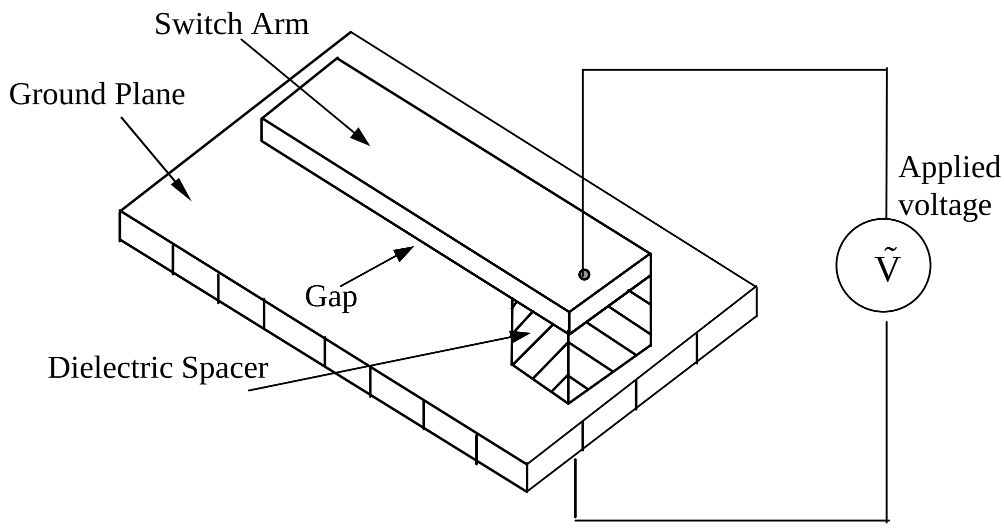

(a)

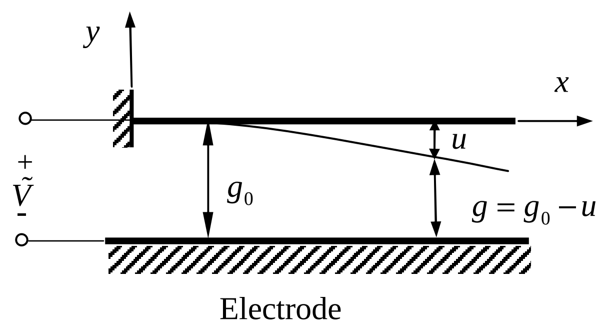

(b)

Figure 2 A cantilever microswitch. a) Undeformed configuration; b) deformation under applied voltage

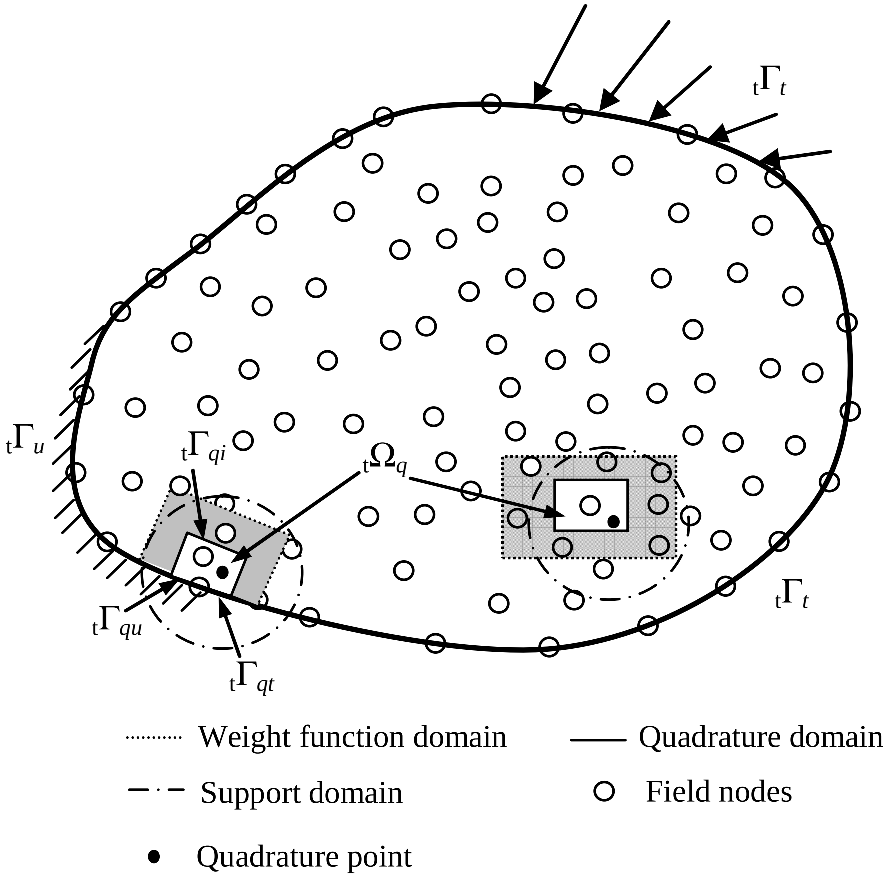

Figure 3 A problem domain and boundaries modeled using the local meshfree method

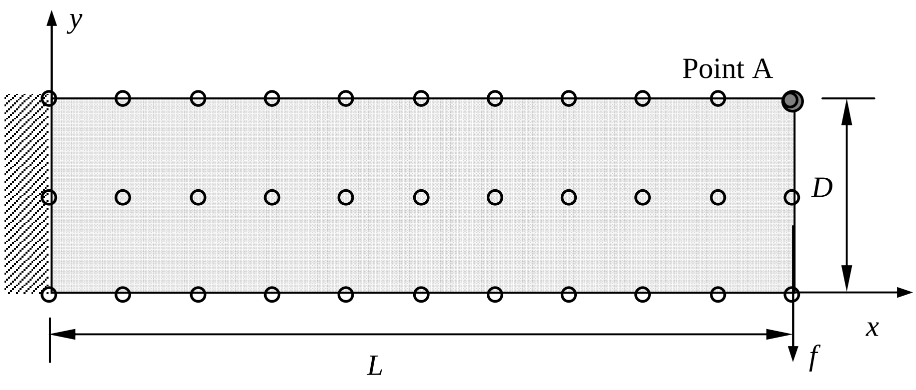

Figure 4 A cantilever beam and the nodal distribution used in the simulation

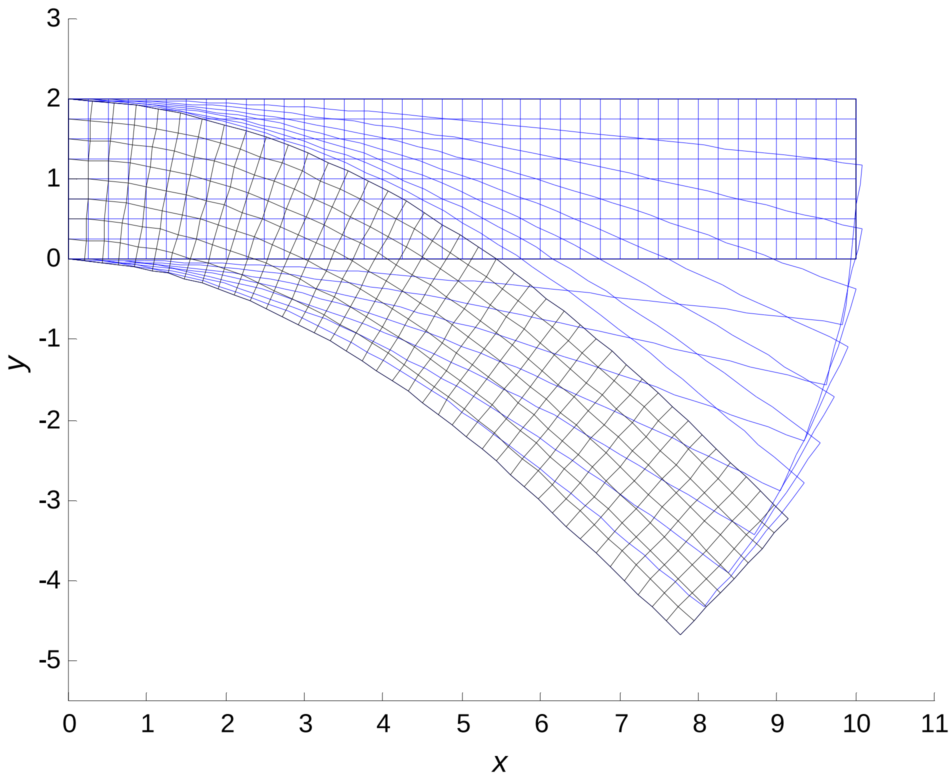

Figure 5 The FEM reference solution for loading steps *N*=8

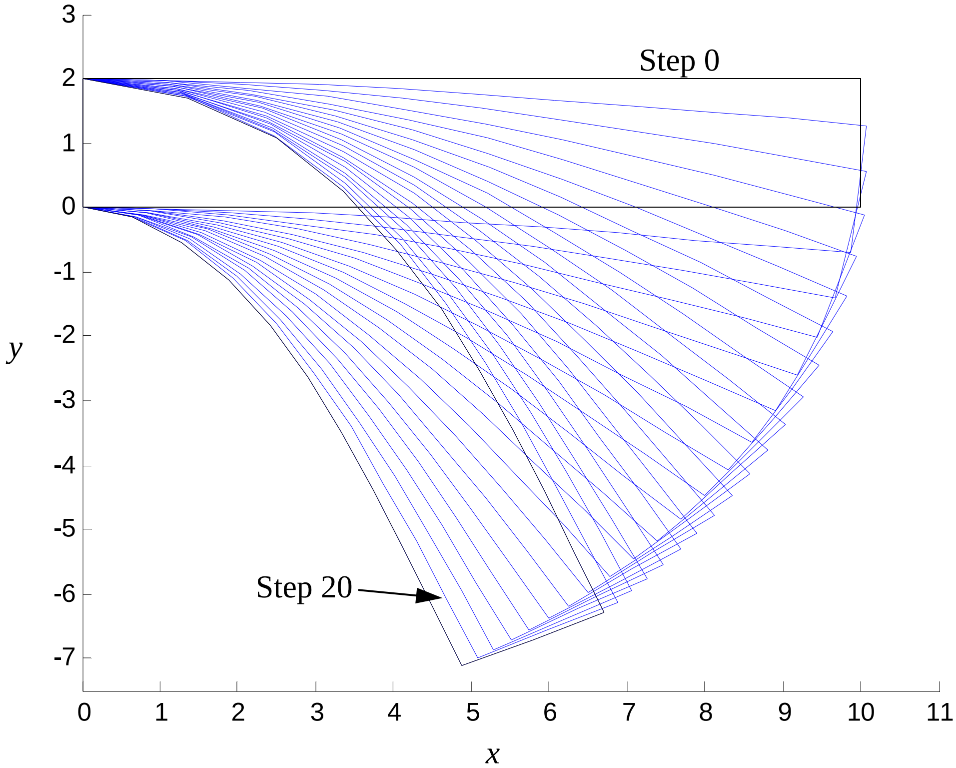

Figure 6 The deflection results for loading steps N=20 using regular nodes

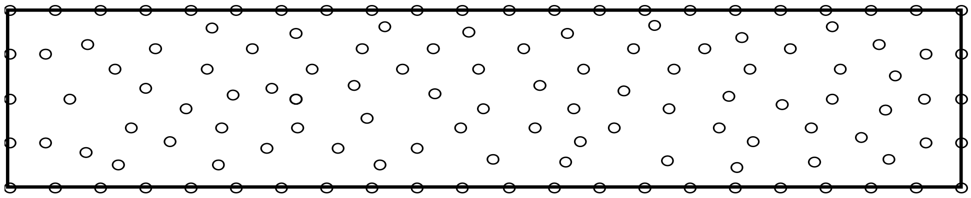

Figure 7 128 irregularly distributed nodes

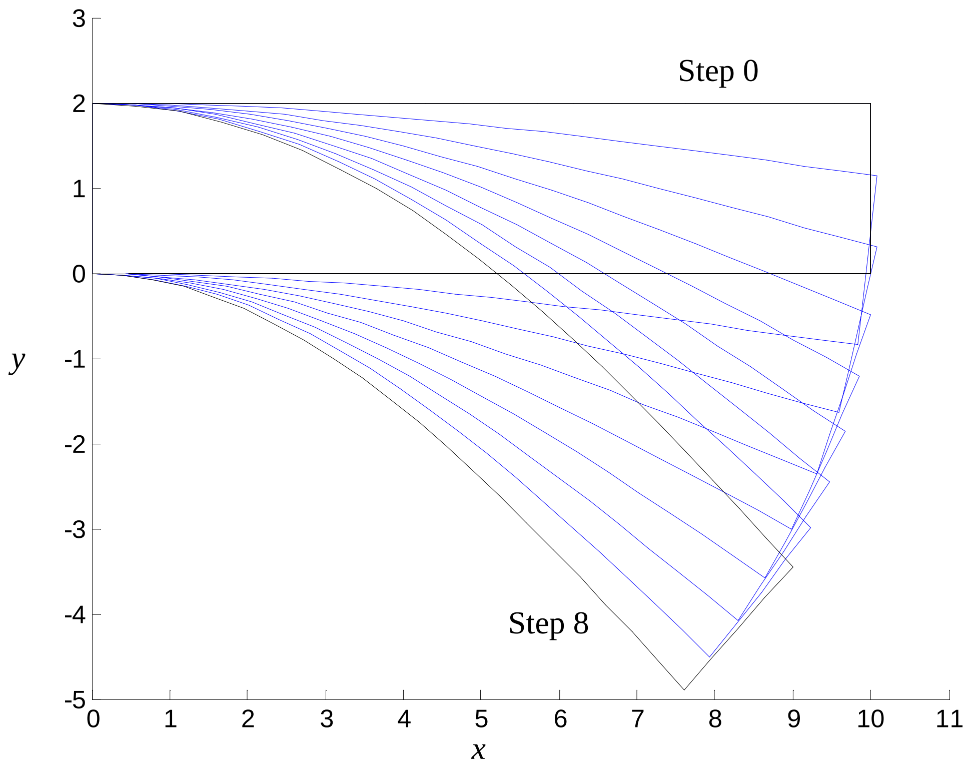

Figure 8 The deflection results for loading steps N=8 using irregular nodes

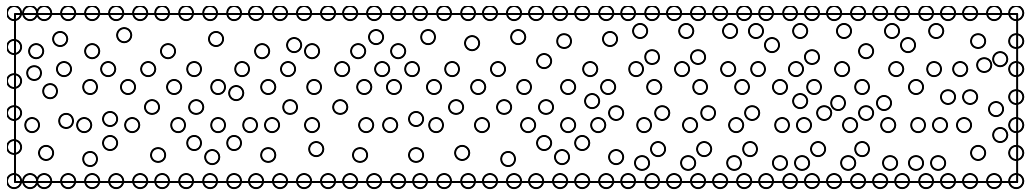

Figure 9 259 irregularly distributed nodes for the microswitch

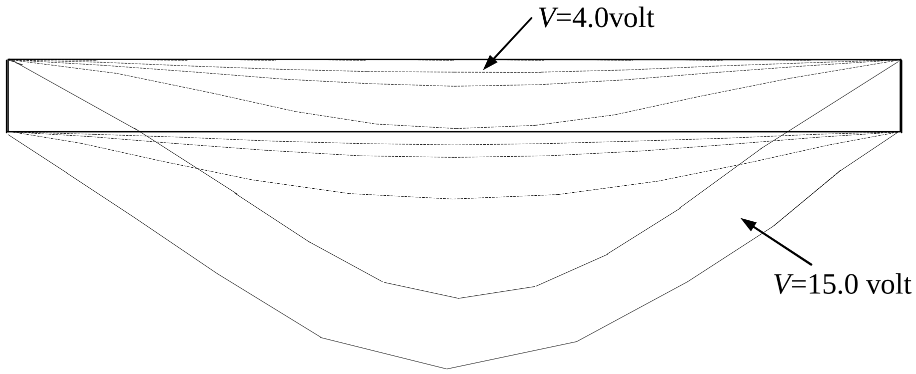

Figure 10 Deflections of the fixed-fixed switch arm under different applied voltages (*V*=4.0, 8.0, 12.0, and 15.0 volt, respectively).

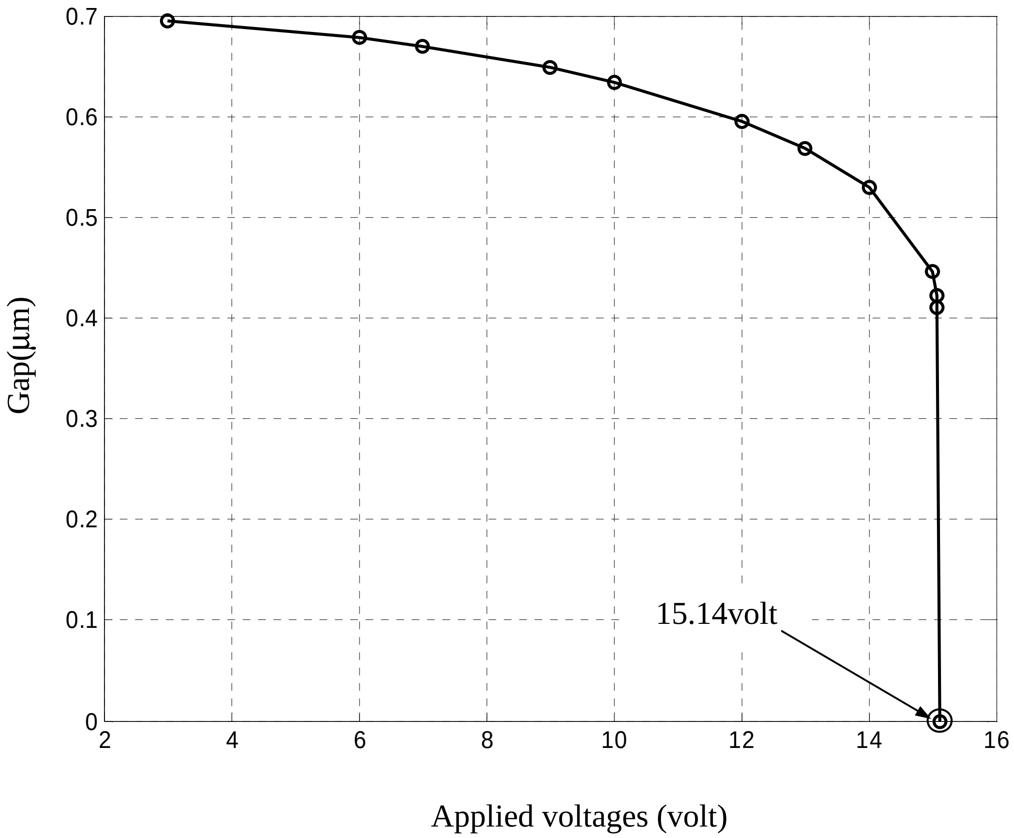

Figure 11 The gap under different applied voltages for the fixed-fixed microswitch

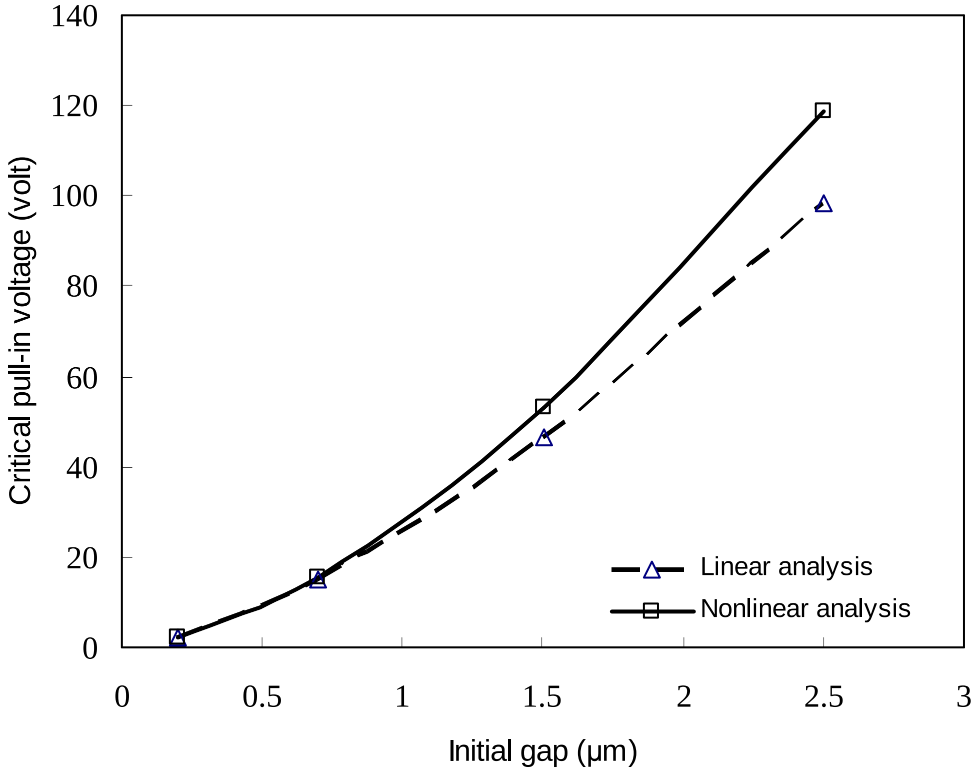

Figure 12 Relationship of the critical pull-in voltage and the initial gap for the fixed-fixed microswitch

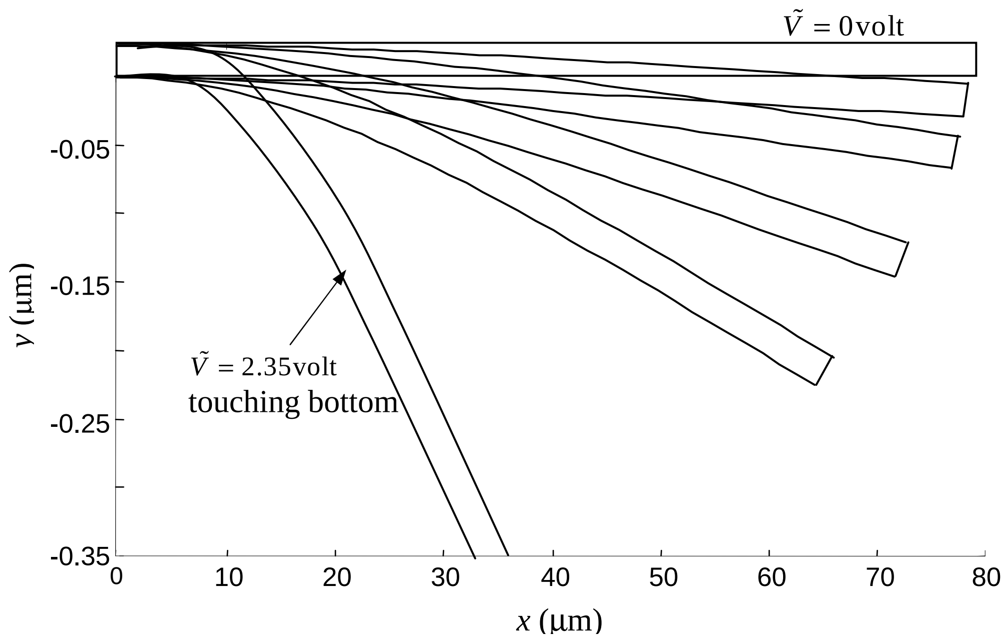

Figure 13 Deflections of the cantilever switch arm under different applied voltages (V=0, 1, 1.5, 2, 2.3, and 2.35 volt, respectively).

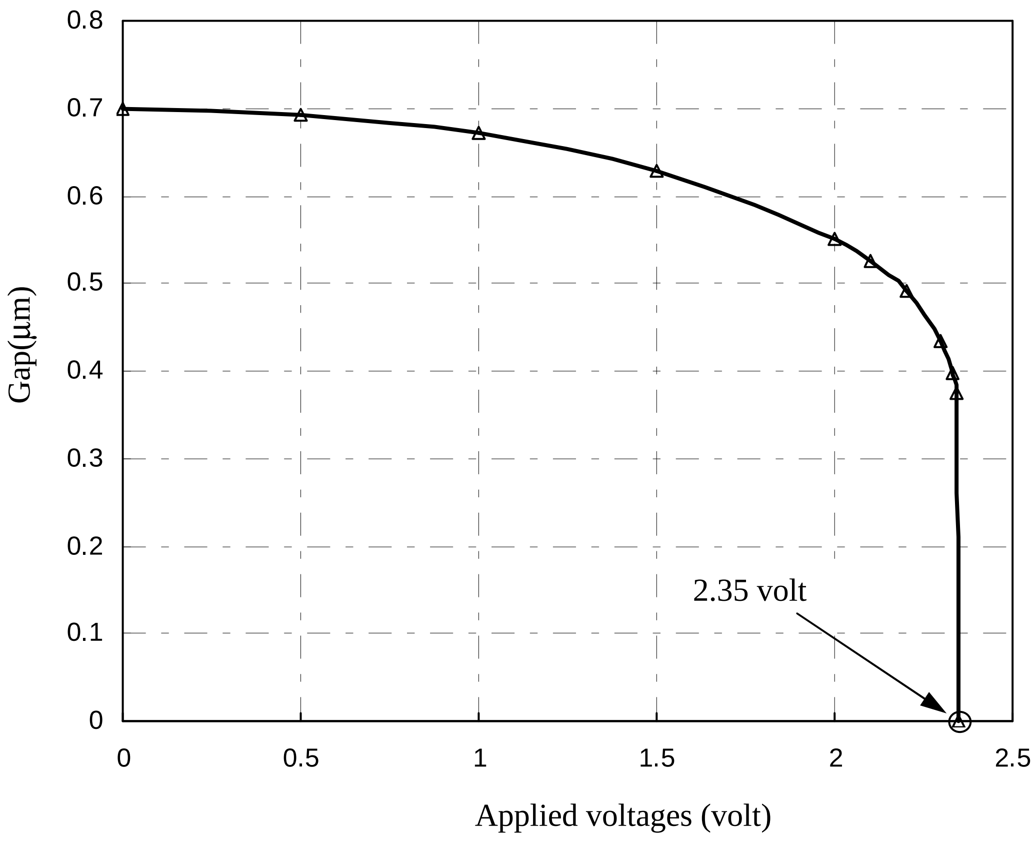

Figure 14 The gap under different applied voltages for the cantilever microswitch

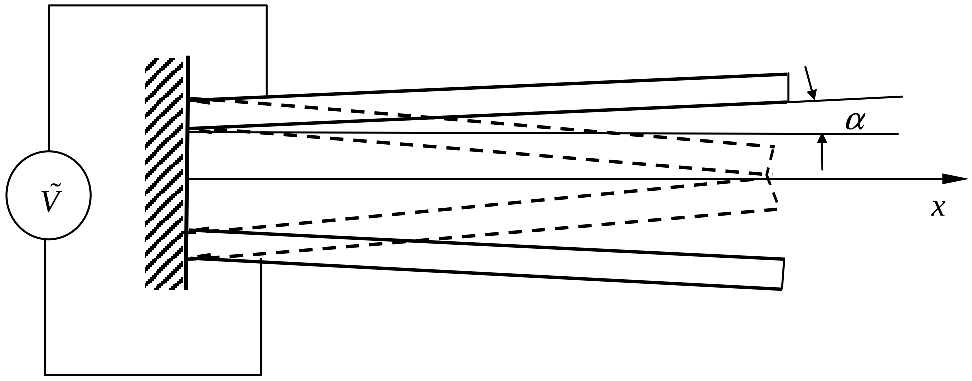

Figure 15 A microtweezer